remote sensing

MDPI

Article

Application of Shore-Based Video and Unmanned Aerial Vehicles (Drones): Complementary Tools for Beach Studies

Donatus Bapentire Angnuureng [1,*], Philip-Neri Jayson-Quashigah [2], Rafael Almar [3], Thomas Christian Stieglitz [4], Edward Jamal Anthony [4], Denis Worlanyo Aheto [1,5] and Kwasi Appeaning Addo [2]

1 ACECoR, Centre for Coastal Management, University of Cape Coast, Cape Coast 00233, Ghana; daheto@ucc.edu.gh
2 Department of Marine and Fisheries Sciences, University of Ghana, P.O. Box LG 99 Legon, Ghana; pjayson-quashigah@st.ug.edu.gh (P.-N.J.-Q.); kappeaningaddo@ug.edu.gh (K.A.A.)
3 IRD-LEGOS, 14 Avenue Edouard Belin, 31400 Toulouse, France; Rafael.almar@ird.fr
4 Aix Marseille University, CNRS, IRD, INRA, Coll France, CEREGE, Aix-en-Provence, CEDEX 04, 13006 Marseille, France; stieglitz@cerege.fr (T.C.S.); anthony@cerege.fr (E.J.A.)
5 Department of Fisheries and Aquatic Sciences, University of Cape Coast, Cape Coast 00233, Ghana
* Correspondence: donatus.angnuureng@ucc.edu.gh; Tel.: +233-244-6-630489

Received: 17 November 2019; Accepted: 21 January 2020; Published: 26 January 2020

Abstract: Video camera systems have been used over nearly three decades to monitor coastal dynamics. They facilitate a high-frequency analysis of spatiotemporal shoreline mobility. Video camera usage to measure beach intertidal profile evolution has not been standardized globally and the capacity to obtain accurate results requires authentication using various techniques. Applications are mostly site specific due to differences in installation. The present study examines the accuracy of intertidal topographic data derived from a video camera system compared to data acquired with unmanned aerial vehicle (UAV, or drone) surveys of a reflective beach. Using one year of 15-min video data and one year of monthly UAV observations, the intertidal profile shows a good agreement. Underestimations of intertidal profile elevations by the camera-based method are possibly linked to the camera view angle, rectification and gaps in data. The resolution of the video-derived intertidal topographic profiles confirmed, however, the suitability of the method in providing beach mobility surveys matching those required for a quantitative analysis of nearshore changes. Beach slopes were found to vary between 0.1 and 0.7, with a steep slope in May to July 2018 and a gentle slope in December 2018. Large but short-scale beach variations occurred between August 2018 and October 2018 and corresponded to relatively high wave events. In one year, this dynamic beach lost 7 m. At this rate, and as also observed at other beaches nearby, important coastal facilities and infrastructure will be prone to erosion. The data suggest that a low-cost shore-based camera, particularly when used in a network along the coast, can produce profile data for effective coastal management in West Africa and elsewhere.

Keywords: intertidal morphology; shoreline change; beach profile; video camera; UAV; coastal management; Dzita

1. Introduction

One general purpose of coastal geomorphological research relates to the development of methods for the consistent estimation of medium-term (order of years) to long-term (decades) nearshore morphology [1]. Preferably, with suitable hydrodynamic forcing and sediment data, these methods

should permit prediction of the behavior of the shoreline and the nearshore topo-bathymetry over time. Furthermore, the effectiveness of these methods would mostly be site specific due to differences in wave and sediment conditions. If structural features or nourishment with sand were situated along the shoreline [2], a more complex method would be required to compute the effectiveness and influences of such modifications within the desired period of time.

Quality data are required for effective coastal evolution studies. For instance, from a laboratory basin or wave flume tank [3], a physical model of a beach profile can be developed. Typically, the prototype is merely scaled down geometrically, by multiplying all the dimensions by a given fraction, in order to generate results in the model scale. Nonetheless, determining the complete values conforming to the model outcomes is challenging, partly due to the difficulties of scaling from the laboratory level to the real world, and partially because of the utilization of a wave climate different from that occurring in nature. Beach morphological surveys along the coast of Ghana, West Africa and other coastal areas of the world have always been accomplished through in-situ and topographic measurements using real-time kinematic differential Global Positioning Systems (GPS) [4–6]. In relation to both space and time, these surveys are intermittent, and the area covered is often small. Besides, in-situ measurements are relatively expensive, and this, therefore, can have a limiting effect on the frequency of surveys.

The dynamic nature of beaches requires high temporal resolution monitoring to appreciate the physical processes that drive change in support of coastal management. This makes video monitoring techniques [7–10] a more reliable option, with advances in the use of this technique over the last decades. One of the products from the video technique, time-averaged images, gives the required resolution to monitor features, such as the shoreline and nearshore intertidal bathymetry [11,12], among others. The application of the video camera system is not standardized, and installation procedures are generally site specific. Despite decades of implementation of the method, first in developed countries, and then less developed countries, there are no standards regarding the altitudinal deployment of camera systems, which are invariably mounted at different elevations (e.g., [13,14]). Based on the elevation and orientation of the camera to the beach, there are variations between the camera observation and the actual target. Currently, camera systems therefore need to be used alongside additional tools in order to attain a high video potential.

The use of camera systems for monitoring beaches is relatively new in the West African region, and, to our knowledge, has been implemented on only seven different beaches in four countries: Benin [14,15] and Ghana [16,17], with recent deployments in Senegal and Cameroon. These camera systems have served as important sources of data for monitoring coastal erosion [15,18]. However, significant improvement is required for most of the products generated. The citation of the local sites is to emphasize the use of Video Camera Systems (VCS) in the region and the need for a regional network for coastal monitoring.

At the same time, small manned aerial vehicles (MAVs), and increasingly, unmanned aerial vehicles (UAVs, also called drones), which also carry cameras, and which are more affordable and easier to run, have become a popular option, with the main products being orthophotos and Digital Elevation Models (DEMs) [19,20]. Aerial vehicles cover larger areas than site-located video cameras but may not be able to provide the very fine temporal resolution accessible with the video technique (see Table 1 for a detailed comparison). Studies have shown that DEMs generated using data from these vehicles are capable of producing vertical accuracies less than 10 cm [21], enabling access to fine-scale beach morphological changes and bathymetry [22]. Orthophotos from these surveys can achieve very high resolution, enabling the study of features, such as beach cusps, as well as the monitoring of intertidal dynamics, among others [23–25]. This high level of resolution is not only good for most engineering projects [26] but could also be used to correct video camera data. The video system implementation is quite different from the UAV-based system for various reasons (Table 1). However, a complimentary application of the two methods will take advantage of the high-frequency data turnout from video and accurate DEMs and orthophotos from unmanned aerial vehicle (UAV).

Table 1. Comparison of video camera (VCS) and UAV-based system.

Item	VCS	UAV
Longshore coverage	<1 km	>1 km
Temporal resolution	Minutes	Days
Elevation above ground	Max 50 m	Can exceed 120 m
Orientation to shoreline	Oblique	Dynamic
Intrinsic error analysis	No GPS system	In-built GPS system
Accuracy	≈ 1 m	<10 cm
Cost	<$1500	>$2000
Risk to user	Safe	Spinning blades
Remote use	Not secured	Secured
Power	Connected to power grid	Runs on batteries
Processing time	Low (light image)	High (dense map)
Rectification of images	Automatic	Manual

In this study, the main objective was to quantify beach topo-bathymetric evolution from a video-camera technique and from data generated by UAV, and compare the performance and complementarities of the two techniques. This information, which is highly relevant for local policy initiatives, is discussed in the context of the improvement of coastal management strategies.

2. Study Area

Dzita beach is located on the eastern coast of Ghana. It is oriented west–east and is about 6 km long. This sandy beach lies ca. 10 km to the east of the Volta river delta, which is one of the largest deltas in West Africa. Adjacent beaches to Dzita beach, including Atorkor and Ada Foah, are both protected with a combination of rock groins and revetments to combat strong erosion, despite the proximity of the mouth of the Volta river, associated with one of the largest deltas in West Africa. The continental shelf off Dzita is narrow (~25–35 km), limited by east–west offsetting by the Romanche fracture zone, a left-lateral transform fault. The Volta delta developed in a large salient trap created by left-lateral offsetting of the coast and continental shelf of Ghana, probably by the Romanche fracture zone [27], a major fracture zone impinging on the Bight of Benin shelf [28]. The wave setting along the coastline is the cyclone- and storm-free West Coast Swell Environment as defined by [29], and the prevailing swells are moderate to high energy (H = 1.36 m), long period (T = 9.6 s) southwesterly swells from the Atlantic [30]. Waves are highest during the boreal summer (June to October). Tides impacting on the coast are semi-diurnal, with a mean range of around 1 m. The mean spring tidal range is about 1.95 m [27]. The longshore sediment drift on this coast is from west to east.

Dzita beach has previously been reported to be eroding. Residents living close to the beach not only complain about regular erosion but also storm surge flooding of their houses. Historically, there has been moderate erosion at the frontage of the eastern beaches of Ghana, including Dzita beach, due to the loss of littoral sediment into the Keta lagoon inlet [31,32]. A shortage of sand-sized bedload supplied to the coast through the main Volta river channel downstream of the Akosombo dam, built between 1961 and 1965, has been highlighted in a number of studies [32–34]. The authors of [32] reported the following rates of shoreline retreat in Keta (Figure 1): 4 m/year 1923 and 1949; 6 m/year between 1959 and 1975; with a net increase after 1964 to between 8 and 10 m/year following the construction of the Akosombo dam. The authors of [4] reported a rise in the mean erosion rate downdrift of the sea defense system of Keta to 17.00 ± 0.3 m/year, following the construction of the seven groin ripraps designed to block longshore transport. The authors of [34] emphasized the fast erosion now affecting this part of the Volta delta coast.

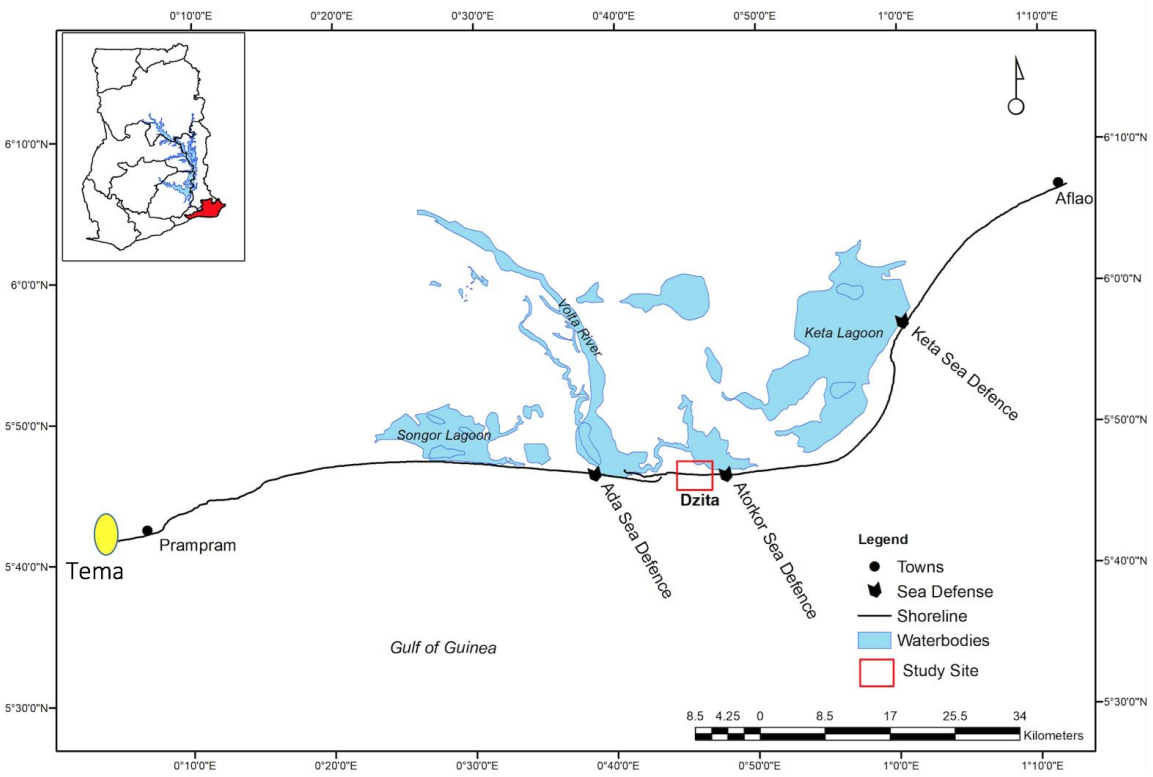

Figure 1. Location of the Dzita study site, with Ghana in the inset. Indicated in yellow is Tema, where the tidal substation is located.

3. Materials and Methods

3.1. Camera Video Data Collection

A video camera with a 180° field of view was mounted on a 13-m-high pole (Figure 2a) erected on the backshore of the beach in April 2018. The camera was mounted and inclined towards the beach at an angle of about 20° to the north to allow imaging of the beach and the surf zone. The spatial coverage of the camera was about 1 km in the across shore direction and 2 km in the alongshore direction, and it was set to record during daylight hours at 2 Hz. The processed beach area on each image was approximately 250 m wide.

Three different types of images were created every 15 min. These are snapshot (Figure 2b), time exposure or timex (Figure 2c), and timestack (Figure 2d) images. The timex image is an average of snapshot images [8] of each 15-min set of snapshots with a 7552 × 1416-pixel length. A timestack image is obtained by stacking a single cross-shore profile for 15-min snapshots of a region of interest to obtain an image. Note that the cross-shore length of the timestack image is different from the cross-shore length of the instant and timex images because only a region of interest (that covers portions of the beach and water) is captured to create the timestack. Timestack images are commonly used for the purposes of wave parameter estimation due to the visible features of breaking waves. Over 11 months of 15-min image data were collected, though these included several data gaps due to camera malfunction periods.

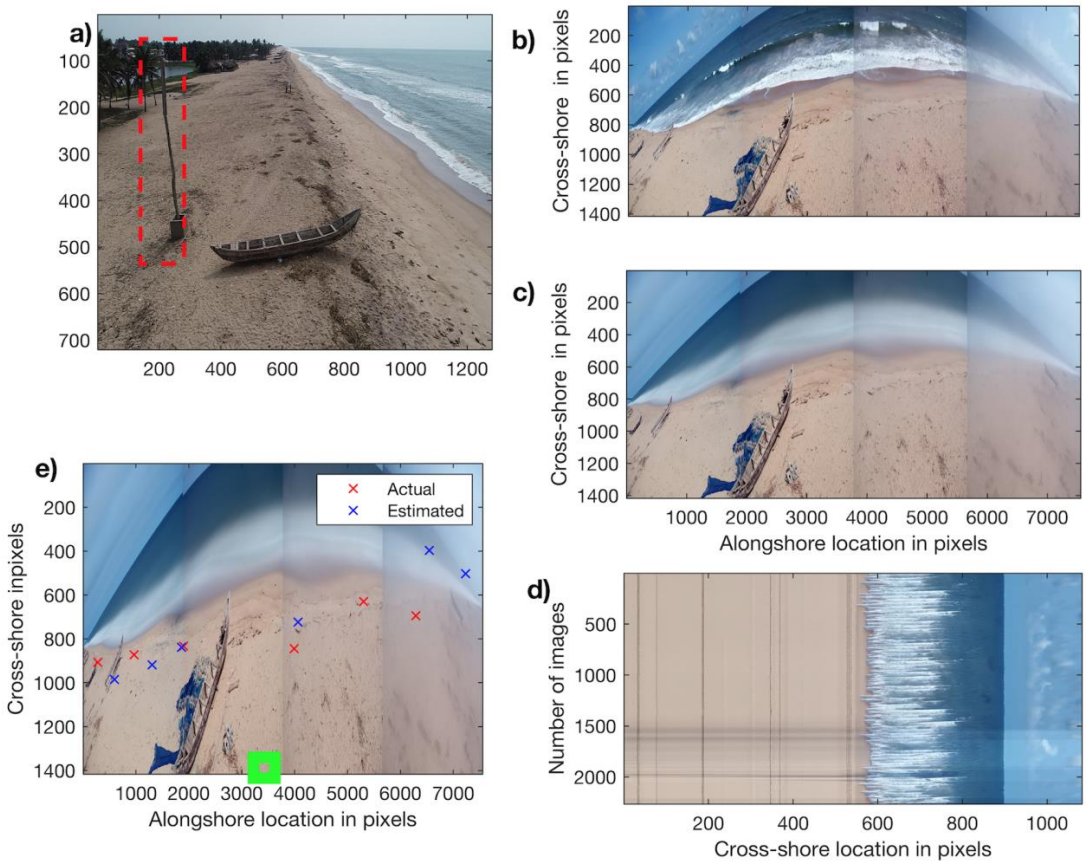

Figure 2. Data from video camera and image characteristics: (**a**) camera installation; (**b**) instant image; (**c**) timex image; (**d**) timestack; (**e**) Ground control points (GCPs) to be used for georeferencing shoreline data from pixel to metric coordinates.

3.2. Orthophoto and DEM Generation from UAV Photogrammetry

Monthly beach UAV flights were carried out on 1 km of the beach using a DJI Phantom 4 Pro drone through a period of one year. Flights were taken at an elevation of 70 m above ground level overlooking the beach. Maximum flight speed was 5 m/s and the total number of transects on each flight path was 30. Prior to the surveys, eight ground control points (GCPs), as seen in Figure 3 (lower panel), were established on the beach and synchronized to the national grid using RTK-DGPS, and used in rectifying the drone imagery [17]. The flights spanned from May 2018 to May 2019 with 10 flights, and a flight per month except for July 2018 and February 2019 when technical problems led to flight cancellations. Flight times, tides and wave height conditions during each day of flight are presented in Table 2. The tidal range is higher than the wave height variation observed at the study site. It is important to note that neap tides could occur at night and this could influence the tide value at the time of flights as indicated in Table 2. An average of 215 images were taken during each flight time. These images were manually filtered to remove blurred or overexposed ones, as well as those that filmed the landing gear of the drone as a consequence of strong winds.

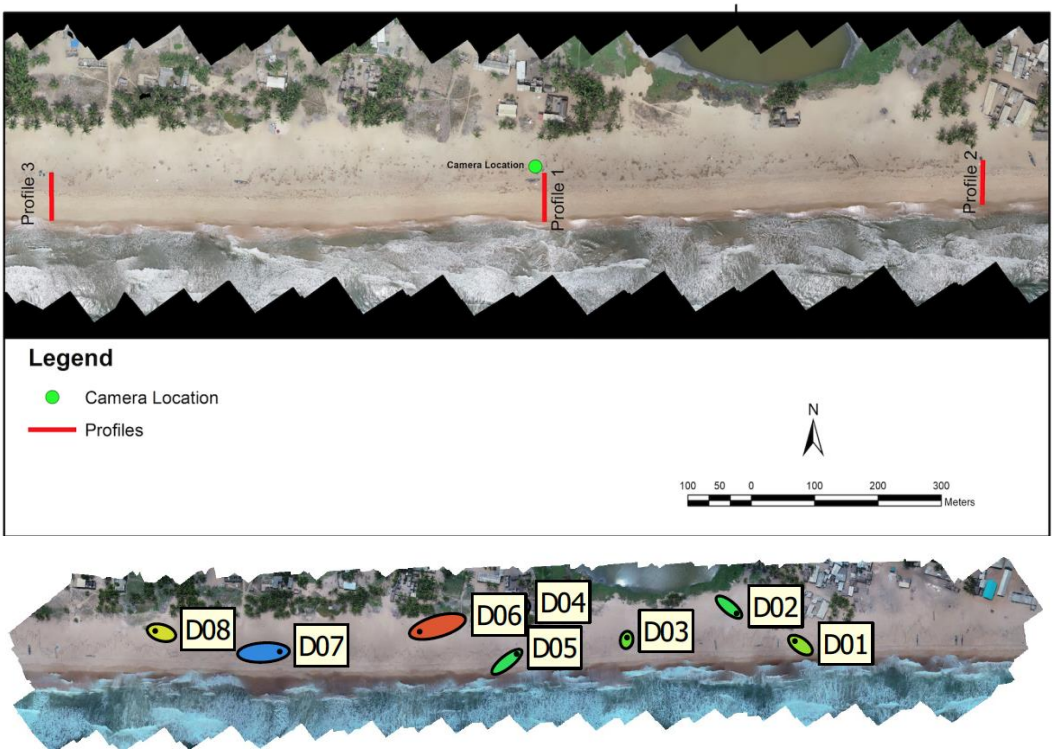

Figure 3. Upper panel: An orthophoto built from 215 images showing three profile locations. Topography is extracted from profile 1. Lower panel: GCP locations on the beach for each flight.

Table 2. UAV Flight times, tides and hydrodynamic conditions.

Date of Survey	Tide at Time of Flight	Max. Tide (m)	Min. Tide (m)	Max. Hs (m)	Min. Hs (m)
29/05/2018	0.40	1.39	0.10	2.20	1.92
28/06/2018	0.77	1.32	0.09	1.85	1.68
07/08/2018	1.29	1.30	0.26	2.40	2.21
07/09/2018	1.07	1.39	0.12	2.00	1.68
04/10/2018	1.20	1.26	0.37	1.32	1.17
08/11/2018	0.19	1.59	0.16	1.52	1.42
11/12/2018	0.29	1.38	0.28	1.72	1.60
07/01/2019	0.27	1.45	0.21	1.65	1.45
01/03/2019	0.77	1.16	0.51	1.22	0.98

Three-dimensional (3-D) scene reconstruction was performed using the method of structure-from-motion (SfM) [35] and multi-view stereo (MVS) algorithms [36] and implemented in Agisoft Photoscan software [37]. The SfM analysis involves image realignment [38], where matching features that are resilient to changes in image scaling and rotation and partially invariant to illumination conditions and the camera viewpoint are identified in each image [24]. Subsequently, the identified features are bundle adjusted to reconstruct a 3-D sparse point cloud. The resulting sparse cloud is then densified through clustering using multi-view stereopsis [35,39] and used to build an orthophoto (Figure 3) and a digital elevation model (DEM). The DEM is classified to extract, as much as possible, only bare ground, and excludes artificial objects on the beach (including fishing boats and buildings). A standard DEM of difference (DoD) approach was used to assess intertidal morphological variations [40]. The DoD was generated by subtracting the earlier DEM from a newer DEM given as:

$$\Delta DEM = k_2 - k_1, \quad (1)$$

where 'ΔDEM' is the DoD, k_2 is the recent DEM, and k_1 is the older DEM.

The profiles of the beach were extracted from the lower foreshore to the berm crest (Figure 3). The profile evolution from the berm crest to the lower foreshore was estimated for each month to reveal

the total beach profile variation. To estimate the horizontal shoreline mobility, alongshore shoreline locations were manually digitized from each of the orthophotos in ARCGIS. The high watermark (HWM) [41] was adopted as the shoreline proxy for the shoreline position in order to be consistent with the marker used for shoreline analyses in the region [4–6,17]. The variations of the monthly shoreline locations were then determined.

4. Results

4.1. VCS Shorelines, Hydrodynamic, and Tide Data

A single profile was extracted from each timex image between pixel points P_1 (3402, 38) and P_2 (3298, 1315). These profiles were then stacked to form another timestack as presented in Figure 4. The authors of [13] have shown that beach sand displays high red coloration (R) and low green (G) pigments, thus yielding a high ratio of R to G, while water pixels display strong green-channel values than low red values nearshore and yield a low ratio of R to G. In Figure 4, the ratio of R to G is computed for all pixels. These low and high ratio values of R to G mark water and beach across shore, based on some bimodal distribution [13]. The local minimum of this distribution curve represents the transition between water and beach, that is, the shoreline. In other words, the shoreline is represented by the time-averaged waterline where the ratio is unity. In Figure 4, the automatically delineated shoreline location is shown (black line) based on the ratios. These data were converted to metric values by geo-referencing with six GCPs collected around the stack pixel location [13]. To improve accuracy, where the ratio is below 0.98 or greater than 1.1, no shoreline was extracted.

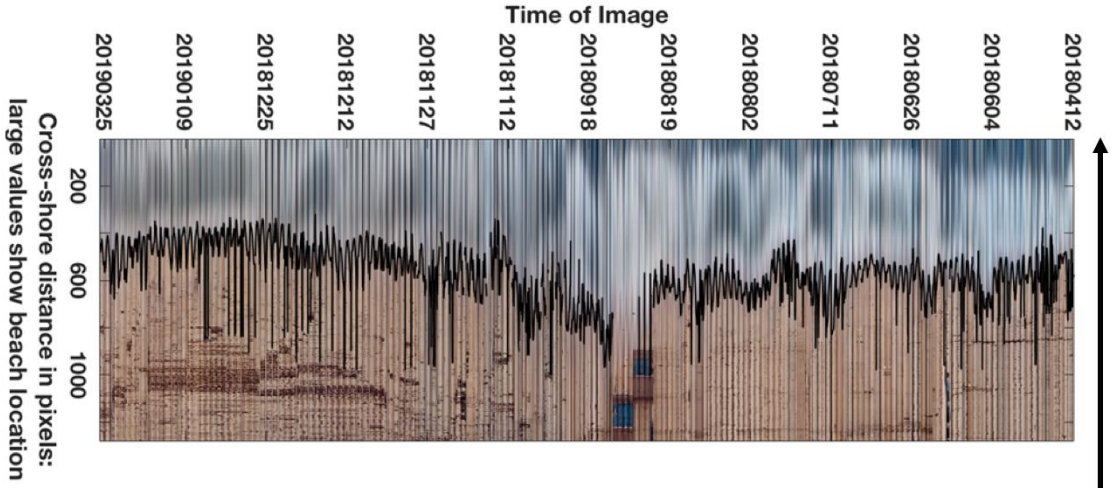

Figure 4. Time stack image from timex images. The black line represents the shoreline location. The arrow points towards the sea from the beach.

Figure 5 shows the hydrodynamic and shoreline data covering the study period. Monthly shoreline locations extracted from VCS ranged from 0 to 15 m (Figure 5a) while hourly shoreline locations reached a maximum value of 40 m off the camera location. Shoreline positions show recession in the austral winter (June to October) and advance in the boreal summer (October to March). Similarly, monthly shorelines extracted from UAV show recession of up to about 9 m and accretion of up to about 15 m over the period. Hourly significant wave heights (Figure 5b) and peak wave periods (Figure 5c) were extracted from ERA5 [42] for the shoreline location of Ghana. Hindcast wave data, including offshore significant wave height, *Hs*, direction, and peak period, *Tp*, were obtained from ERA5 global reanalysis [43] between latitudes 1.5° *n* and 7° *n* and longitudes 1° W and 2° E. ERA5 is the fifth-generation atmospheric reanalyses of the global climate produced by the European Centre for Medium-Range Weather Forecasts, which has added different characteristics to a previous model, ERA-Interim. The ERA5 data released so far cover the period from January 1 1979 to near real time.

The ERA5 that is being developed through the Copernicus Climate Change Service (C3S) has improved the spatio-temporal resolution to hourly time intervals and the horizontal resolution to 31 km, with 137 levels up to 0.01 hPa. A number of gridded variables are available under ERA5, but for this current paper, we used *H*s and (*T*p) for the period of May 2018 to May 2019. Data are open access and free to download for all uses.

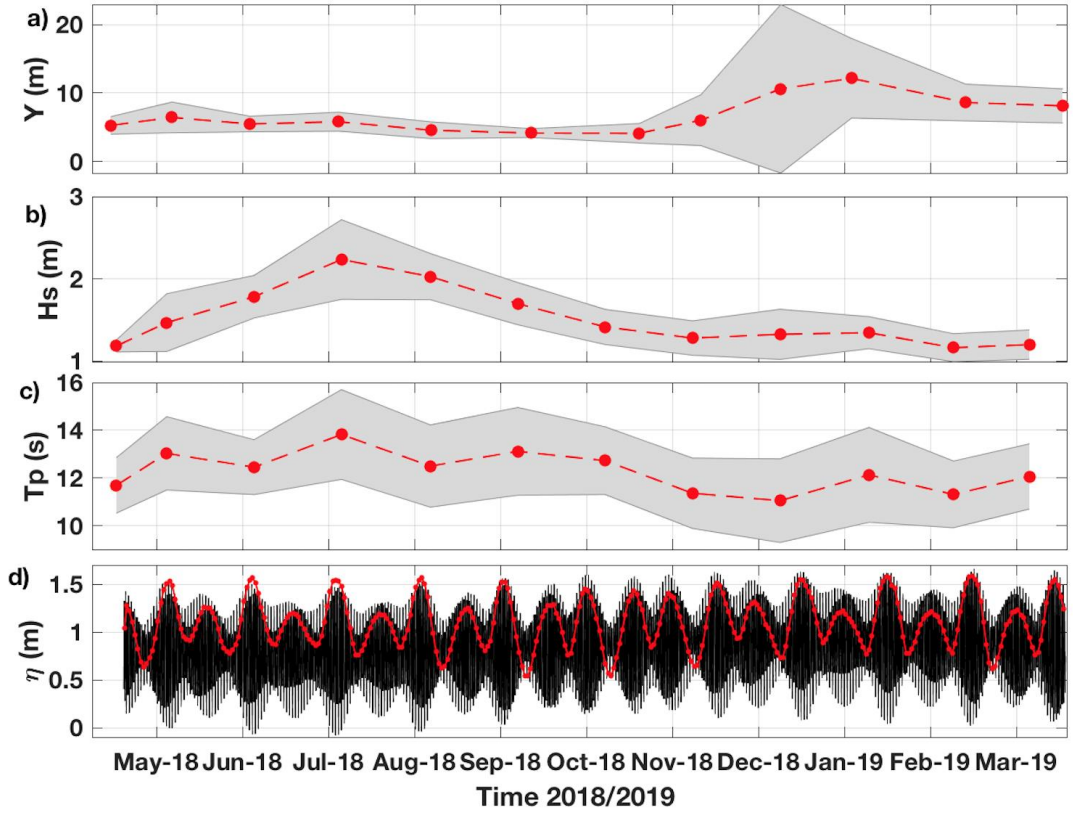

Figure 5. (**a**) Alongshore-averaged shoreline positions (*Y*); (**b**) significant wave height (Hs); (**c**) peak period (Tp); (**d**) 15-min tide values (water levels) with daily tide range overlain. Shaded areas represent the variation/standard deviation of data.

In addition, astronomical tides (Figure 5d) were obtained from the WXtide32 prediction program [44]. The WXTide32 program predicts tides from 1970 through to 2037, for more than 9500 tide gauge stations worldwide. In Ghana, the main tide station is located at Takoradi, which is over 300 km west of Dzita. Therefore, because there is no tide gauge at Dzita and in order to reduce lags in the tide variation, the tidal subordinate/substation at Tema (marked in Figure 1), which is about 80 km from Dzita, was used as the reference point. Tide data were downloaded at 15-min intervals i.e., at the same interval as video shoreline data (Figure 5a). Tidal amplitudes extracted from the WXTide32 program vary from 0 to 1.7 m (Figure 5d) while the mean tide range during this period is 1.1 m.

4.2. UAV Data

DEMs and orthophotos generated from UAV data covered approximately 1 km long alongshore, and fully covered the same part of the ca. 80 m wide open beach in the cross-shore direction in each campaign. The VCS camera was located in the center of the covered section. The DEM resolution was 7.5 cm for most campaigns, and 12 cm for April, May, and June 2019. Maximum (minimum) uncertainties in the height (Z) and position (combined XY) were 18.9 (0.8) and 45.9 (6.9) cm respectively, as calculated from the Photoscan standard protocol (for ground control points). During all campaigns, fore-shore (intertidal) slope and beach berm are prominently visible in the data.

4.3. Comparative Shoreline Locations from VCS and UAV Data

Alongshore-averaged shoreline locations (*Y*) extracted from the UAV orthophotos over the 1 km of the surveyed area and VCS timex images are presented in Figure 6a. Lower shoreline locations represent a recession of the shoreline. Larger values are farther seaward, representing significant beach accretion. In the VCS data, the intertidal shoreline locations vary from 4 to 12 m (Figure 6) over all the months. Similarly, monthly shoreline locations extracted from UAV show variations ranging between 7 and 17 m over the period. The lower shoreline locations represent recession of the shoreline. The correlation coefficient, r, is 0.73 between monthly VCS shoreline locations and UAV shoreline locations (Figure 6b). The UAV shorelines correlate with the VCS shoreline positions, with an R^2 of 0.50. A slight deviation from the 1:1 line was observed. The VCS shoreline locations are overestimated during shoreline recession and underestimated during shoreline advance. A shoreline length difference of about 3.5 m is observed throughout the period of study between the two methods. This is probably due to the resolution in the VCS data estimation. Both VCS and UAV data are influenced by wave-induced set up but the total error in the VCS data also includes resolution based on rectification, water level variation and camera height. The cross-shore resolution (or error) after rectification was estimated as 1.5 m due to camera location while the overall horizontal error induced by tidal variation is 1.75 m. This additional error of about of 3 m prevails through all the months for UAV vs. VCS shoreline locations (*Y*).

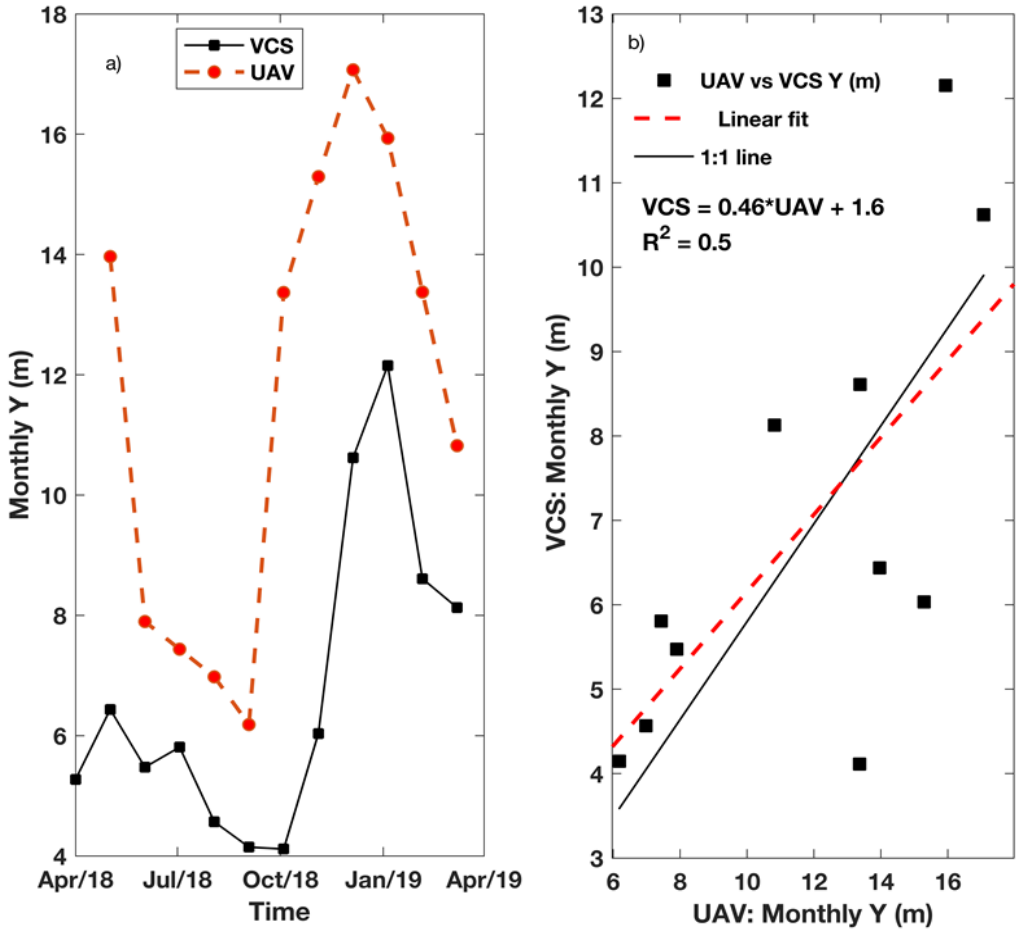

Figure 6. (**a**) Monthly alongshore-averaged shoreline location *Y* extracted in the study period for both UAV and VCS; (**b**) correlation between UAV *Y* data and VCS *Y* data.

4.4. Erosion Rates

The data show that the months of September to October 2019, as in Figure 5a, were characterized by larger erosion than the other months in the year. Using the data presented in Figure 5a, the rates of shoreline change were estimated from the VCS data from May 2018 to March 2019. The shoreline recession attained a maximum daily value of 25 m during the observation period while the beach advance reached 12 m. Erosion rates were estimated from the VCS shoreline location by using the end point rates where the changes in shoreline between consecutive periods (month to month) were computed. Anticipated coastal erosion can be estimated over some definite time in various ways (e.g., end point rate and linear regression), but this is always subject to ambiguity because of measurement errors, and shortages in the models used to assess historical shoreline position data. The end point rate method uses only two data points—the difference between the earliest and most recent shoreline positions—to yield the change rate [45]. The shorelines used here were that of consecutive months. Shoreline change (ΔY) rates for VCS shorelines range from –3 m/month to 7 m/month (Figure 7).

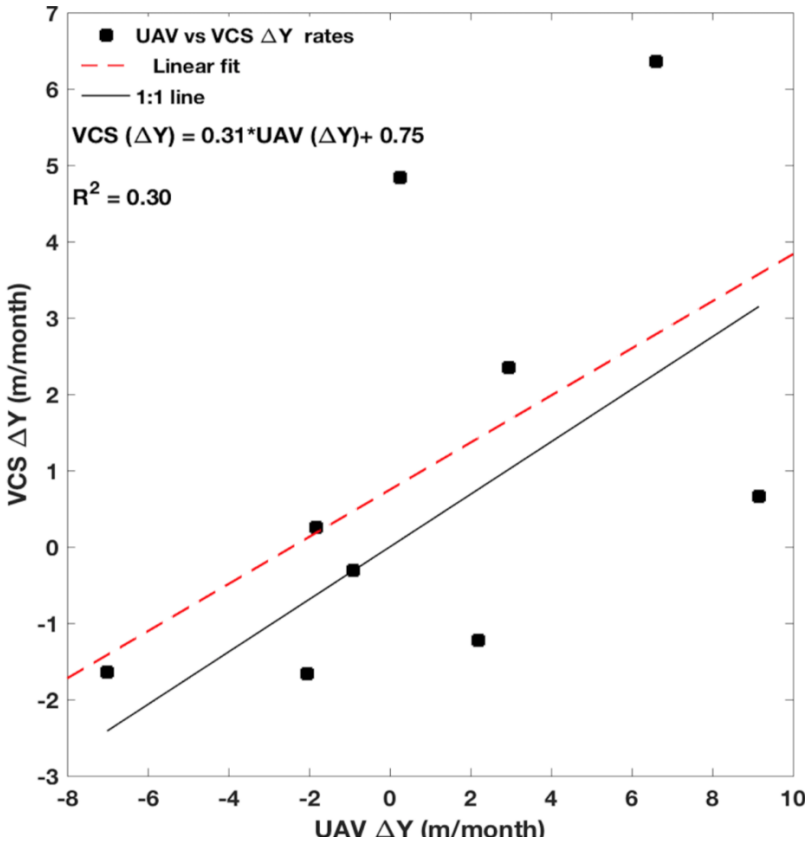

Figure 7. Correlation between the shoreline positional changes (ΔY) of VCS and the UAV for each consecutive monthly measurement. Negative values mean erosion while positive values represent accretion.

Figure 7 presents a scatter plot of the shoreline change rates per month estimated using the end point rate method [45]. The correlation coefficient, r, between the shoreline change rates per month for the VCS and UAV results (Figure 7) is 0.55, which is moderately satisfactory. The ΔY for VCS are always overestimated. Deviation from the 1:1 line was observed. The slope (=0.31) indicates that the regression line is gentler than the 1:1 ideal regression line. Overall, the estimates for the VCS shoreline change rates is in the same range as the UAV, but high deviations are observed during erosive periods than during accretion periods.

On the other hand, the monthly shoreline analysis from the UAV data show that erosion dominated the entire shoreline (Figure 8), with rates reaching as high as 1 to 4 m over the study year at some locations on the beach. The highest shoreline erosion was observed during the May–August, 2018 period. The May–August, 2018 period corresponds to the high wave-energy season at this beach. The rates of erosion are observed to decrease afterwards with some accretions, except for the period December 2018–March 2019. In addition, Figure 8 shows that the rates were generally lower downdrift (eastward), which is consistent with the sediment transport direction. The rates of cross-shore shoreline change estimated from the UAV data are provided in Table 3. Erosion or accretion values were computed based on two-dimensional horizontal oscillation of the shoreline position between two consecutive months while volume changes relate to the quantity of sediment loss from the foreshore or intertidal zone. The results suggest that the shoreline could experience larger erosion over a full month while sediment that is being eroded is deposited as a low-tide berm due to longshore drift or cross-shore currents [17]. This is what is indicated in the first row of Table 3. The recession of the shoreline could be related to overtopping of the low-tide berm by breaking waves while in essence sediment is accumulating on the lower foreshore. This was not evident in one period only; it was observed in May–August 2018 and December 2018–March 2019, periods during which the shoreline did not experience accretion, yet sediment accumulation was observed on the foreshore surface. The erosion rates calculated over three-month intervals ranged from 1 to about 8 m. Despite intermittent accretion of the beach, from May 2018 to May 2019, the shoreline was characterized by erosion to the tune of about 7 m over the year. Sediment volume losses (Table 3) reached a peak between the months of August and October 2018 whereas the highest deposition/accretion was observed between December 2018 and March 2019.

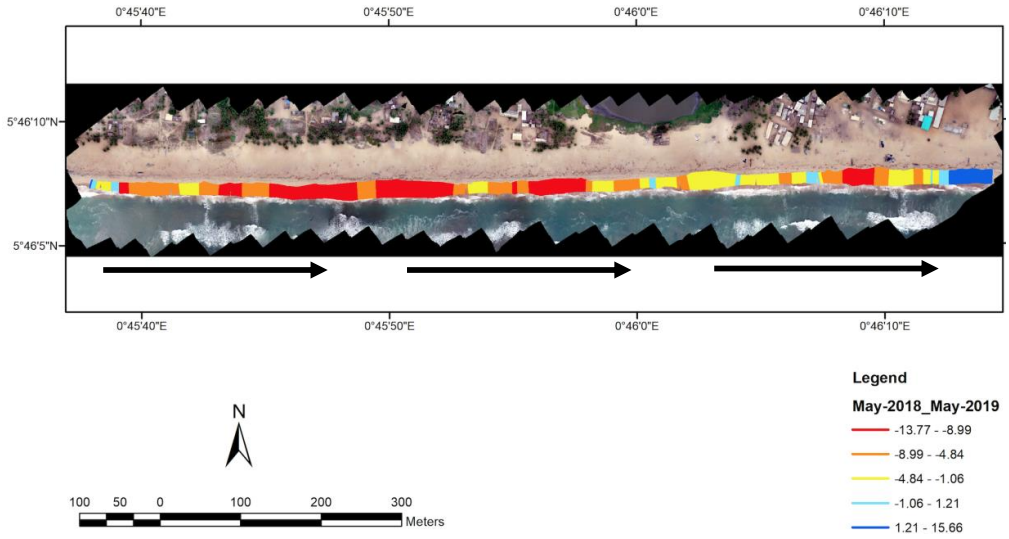

Figure 8. Alongshore shoreline change rates derived from UAV data overlain on an orthophoto. Thick horizontal arrows indicate the drift direction from west to east along the beach.

Table 3. Shoreline change rates and sediment volume variations over the study period from the UAV data.

Period	Shoreline Retreat (m)	Shoreline Accretion (m)	Volume Loss (×1000 m^3)	Volume Gain (×1000 m^3)	Beach Slope
May 2018–Aug 2018	8.27	0.00	0.89	5.80	0.30
Aug 2018–Oct 2018	2.17	5.80	26.85	1.69	0.50
Oct 2018–Dec 2018	1.00	4.45	3.58	5.50	0.10
Dec 2018–Mar 2019	6.73	0.00	0.68	25.88	0.13
Mar 2019–May 2019	2.35	1.58	0.62	9.81	0.20
NET (Full year changes)	7.16	0.38	0.17	11.97	0.25

4.5. Beach Volume Changes

The DEM of difference (DoD) between some of the months during the study period is presented in Figure 9. The figure highlights sand redistribution from the berm crest to the lower foreshore. There is no significant difference between May 2018 and June 2018 (Figure 9), months characterized by moderate wave forcing [16]. From August to October 2018, about 26,850 m^3 of sediment was eroded compared to only 1690 m^3 of deposition. Figure 9 shows a significant accumulation on the lower foreshore from August to September 2018, possibly reflecting the translocation of sand eroded from the berm crest. From October to December 2018, deposition (3600 m^3) and erosion (5500 m^3) were more or less balanced on both the lower foreshore and berm crest (Figure 9). Figure 9 shows that by March 2019, there had been significant sediment accumulation, with the sand distributed over the entire beach.

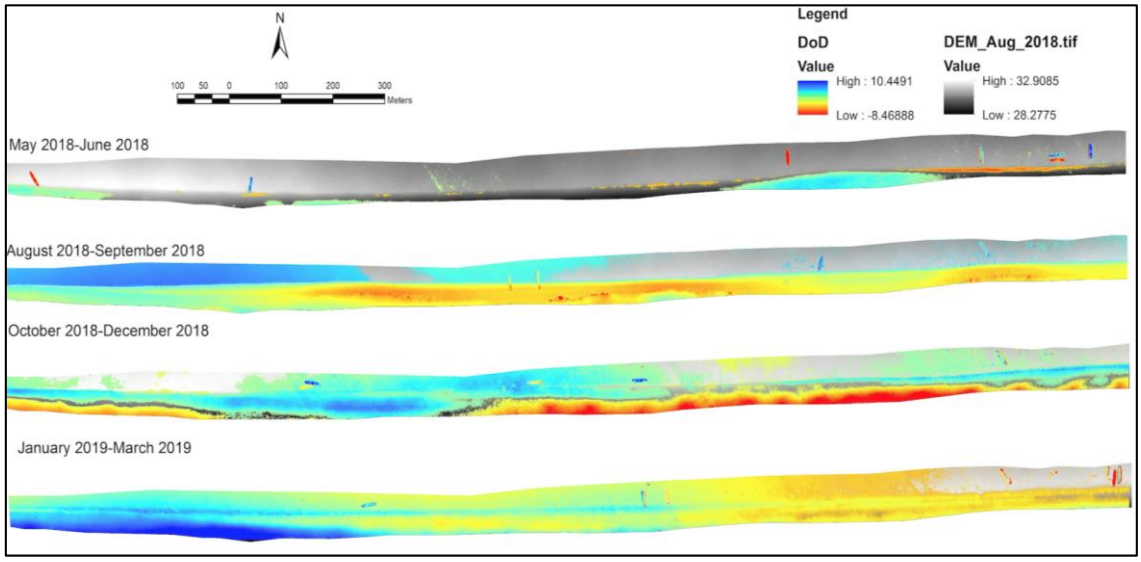

Figure 9. Sediment deposition on the intertidal beach from seasonal DEM of Difference (DoD) for four intervals from May 2018 to March 2019.

4.6. Intertidal Profile Characteristics from VCS and UAV Data

Using several shoreline locations of consecutive video camera images from each month, beach profiles and slopes were determined using linear interpolation and regression of the tide elevations and shoreline locations along a selected intertidal cross-shore distance. On each video image, the shoreline location is rectified to Cartesian coordinates with RTK-GPS GCPs, and water level elevations are extracted at the same time at 15-min intervals. The VCS beach profile at each time is computed by linear interpolation of cross-shore location, corresponding tide value, and regular cross-shore distance with increments at 0.25 m. Full cross-shore distance is defined here as the horizontal distance between the highest water line (high tide) and lowest water line (lowest tide). In this study, a maximum cross-shore distance of 40 m was obtained with respect to the high-water line for all the images. Beach slopes were estimated by regressing the tide elevation with the cross-shore shoreline location.

Beach profiles have been determined using various methods [1,20,22,23]; however, this study is one of the first to combine two complementary methods in order to estimate beach profile variations. The intertidal profiles extracted from the UAV DEMs vs. profiles estimated from VCS are plotted in Figure 10. Individual months from May 2018 to March 2019 are presented. There is an obvious discrepancy in magnitudes of the elevations where profile elevations of the UAV are larger than those of the VCS. The difference in profile elevations between the VCS and UAV suggests that the former is incapable of accurately determining profile elevations. The differences between the two techniques have been outlined in Table 1; the deviations in results are probably due to the tide variation, wave-induced set up, camera oblique view, and view resolution of the VCS. During the rectification

of VCS data, the elevation, z, coordinate in the ground control points (GCPs) is considered constant, and denoted zero, and this could affect the horizontal shoreline distance, which is subsequently used to retrieve the profile elevations. The error associated with the VCS profile elevations due to the shoreline locations (Y) in Figure 6 and the beach slopes in Table 3 as estimated in this study ranges from 1.4 m to 4.6 m. This is revealed in the discrepancies between UAV vs. VCS profiles. Topography derived from UAV photogrammetry is commonly associated with small errors in relative height [23,25]. The average error estimated on DGPS GCPs is approximately 0.25 m. Using the reporting tool in the processing software of photoscan to propagate errors (UAV altitude, image overlap, number of GCPs, etc.) in this study, the uncertainties in the topographic height (z) generated are 0.19 (0.008) m for maximum (minimum), respectively. This is consistent with [25] who found that DJI Phantom 4 gives substantially more accurate model values with a root-mean-square vertical error of 0.05 m. This is small compared to the values obtained for VCS uncertainties. In addition, UAV profiles are directly measured from DEM while VCS profiles are indirectly extracted from a combination of procedures. All profile elevations from UAV range between 0 and 5 m, whereas profiles obtained from VCS range from 0 to 1 m. Further, VCS sets of data are sensitive to profile location; by changing the profile direction or location the correlation with UAV becomes better. As observed in Figure 10, the relation between the two profiles is consistent. This relation is stronger than profiles taken away from the camera location, despite the fact that UAV data were taken at single tide values (at low tides) with a minimal error. UAV data at very low tides ensures wide profile detection because the method fails in the water column. The challenge is, however, that low tides do occur sometimes in the night and UAV data may be obtained at mid-tide during the day (Table 2); furthermore, sometimes, technical issues would result in the missing of low tide windows. Our data are moderately correlated between monthly profiles of the UAV and the VCS data on the berm crest in relation to the alongshore-averaged shoreline locations while the correlation is low further away in the lower part of the intertidal profile. No relation was observed in January 2019 between the VCS and UAV. The difference between the two sets of profiles is estimated with a root mean square error of 0.8 m.

On a daily basis, the data indicate a VCS profile variation of between 0.2 and 1.5 m, but there is a considerable decrease in elevation after the averaging into monthly profiles. Beach slopes estimated from the VCS system showed that except for August and September 2018 when beach profiles were the steepest, with slopes of 0.6 and 0.8, respectively, slopes generally varied between 0 and 0.3. The gentle period of the beach was observed from December 2018 to February 2019, with beach slopes of 0.07, 0.07, and 0.18, respectively. The beach slopes estimated from the UAV DEM profiles range from 0.1 (5.8°) to 0.36 (19°). The average beach slope determined for VCS and UAV is 0.20 (11.3°). These slope values are characteristic of the highly-reflective West African beaches [46,47] with a highly contrasting rainfall regime, especially in the dry season months when the beach water table is low and the wave regime mild. West Africa has, on average, steep slopes, which can be attributed to the swell dominated wave climate along the coast [48]. In addition, the beach slopes were detected for the intertidal zone that has continuous dynamics. The beach slopes observed here are consistent with other beaches in the Bight of Benin, e.g., slope values at Grand-Popo [15,47].

The averaged profile evolution of the VCS and UAV systems during the entire study period portray a VCS and UAV profile intersection on a cross-shoreline location of about 6 m (Figure 11). It is of interest to note that at this location, the upper limits of the standard deviation switched, becoming the lower limits indicating the presence of a beach feature such as the accumulation of sand into a sandbar. The data shows a significant overestimation by the VCS in the nearshore, and underestimation seaward.

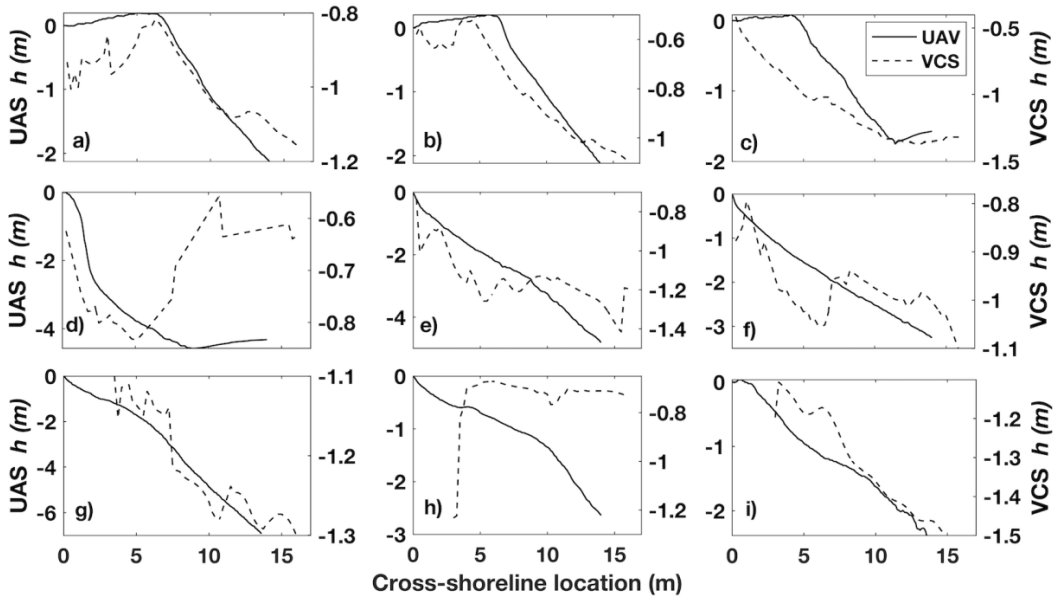

Figure 10. Beach profile elevations *h* from UAV (solid lines) and VCS (dotted line): (**a**) May 2018; (**b**) June 2018; (**c**) August 2018; (**d**) September 2018; (**e**) October 2018; (**f**) November 2018; (**g**) December 2018; (**h**) January 2019; and (**i**) March 2018.

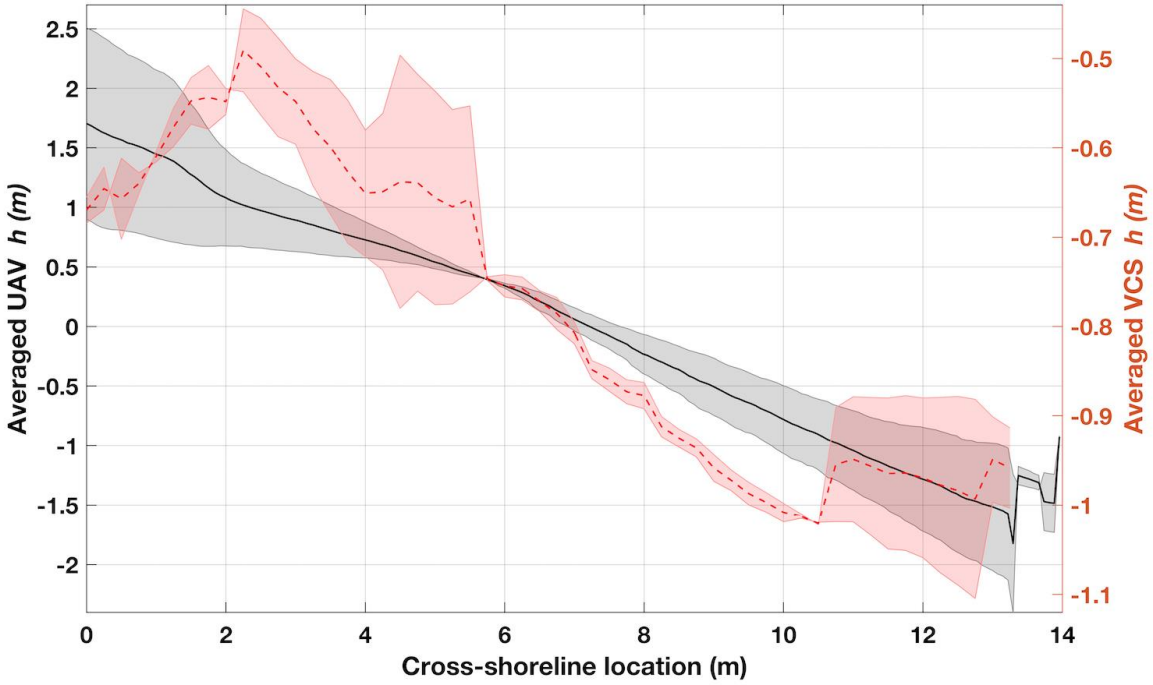

Figure 11. Averaged cross-shore beach profile elevations *h* for VCS and UAV data. Shaded regions represent the monthly standard deviations.

5. Discussion

Several survey methods can be used for the quantification of nearshore intertidal topography and bathymetry, including echosounder, Light Detection and Ranging (LiDAR) surveys, satellites, and UAV and VCS systems. The video camera systems have the ability to capture a large number of incident waves with multiple frames per second. Due to the duration of the VCS and UAV, errors are limited to tens of centimeters [49]. One of the high-resolution satellite images, Sentinel1, and more recently Sentinel2, is characterized by a spatial and temporal resolution of about 10-20 m and 5 days,

respectively. Given that all the shoreline locations in the current paper are less than 20 m, they are lower than the satellite data resolution, thus they are poor for all the shoreline location detection.

Wave conditions may not be the predominant controlling factor along this beach [16]; however, Figure 5 shows the shoreline variation is inversely related to the hydrodynamic conditions. The data show that increasing wave heights from June to October 2018 correspond to low magnitudes of shoreline location, which signifies that the shoreline retreats more landward in the austral winter. It is evident that the data extracted from the VCS technique moderately represent beach conditions. These data also reveal the beach advances in the austral summer when low wave conditions prevail. This prevalence of low waves is consistent with conditions along most equatorial to south Atlantic coasts [50], in contrast to coasts in the north Atlantic and higher latitudes where relatively low wave heights are observed in summer (June to September 2018).

The cumulative shoreline erosion observed using the VCS method is small (1.5 m/year) compared to that obtained from the UAV data (7 m/year). The fact that short-scale alongshore variations of the shoreline and intertidal bathymetry are not well resolved with this technique (Figure 11) suggests that the VCS profile estimation is possibly influenced by: (1) Gaps in the VCS data; due to power outages, the video camera was not operational at some points in time and also foggy images were not utilized; and (2) oblique views of the VCS camera. Figure 11 shows a spatial lag of 2 m in the cross-shore between the VCS and UAV. This is probably due to the difference in the frequency of the two data sets collected. UAV data is taken only once a month in comparison to VCS, which is taken almost every 15 min. Because UAV data is only once a month, short-term variations due to wave overtopping or tidal surges may not be observed during the survey time. This indicates the relevance of short-scale studies [51]. The monitoring of foreshore features in medium to high energetic coastal environments require remote sensing data with specific characteristics [22,23]. Temporal frequency is a crucial factor, since it can improve the results. A good correlation between VCS and UAV profile surveys was observed, showing that the proposed approaches can be complementarily used and are relatively cost effective.

The camera was inclined towards the beach at about 20 degrees and only about 13 m above ground level in contrast to the UAV, which was flown at 70 m above ground level and perpendicular to the shoreline. Though shoreline locations were transformed using standard photogrammetric principles, it is widely assumed that the camera elevation affects the estimated data. Conveniently, at large ranges from the camera location, short-scale variability is suppressed by the coarsening of the image pixel resolution [52]. Unless the beach is truly planar, the intertidal profile estimates may tend to be increasingly uncorrelated to the observed UAV profiles. When faced with this situation, an obvious way of limiting the error magnitude would be to limit the analysis to images corresponding to relatively low wave heights [52], which were not considered in this study.

At the current retreat rate (7 m/year), and without any engineering intervention, an estimated area of 200 m of beach and backshore would be eroded in the next 30 years. The sand deficit affecting the still natural sandy beach of Dzita, located between the sea defense sector of Atokor and the mouth of the Volta River, may increase in the future. This rate of erosion has been measured along the eastern coast of Ghana since 1960 [4,32–34]. One of the main objectives of the Keta Sea Defense was to protect the major road in the district. Erosion poses an immediate threat to the road linking Anyanui and Atorkor as well as to other infrastructure, several houses, a school, and a guest house.

The data show that beach slopes are larger down the berm crest, illustrating the reflective (slope >0.1) character [30] of this erosional beach during austral winter, and a propensity for downslope transfer of sand removed from this beach face to a gentle lower foreshore, where there is evidence for accumulation (Figure 9), indicating also a predominantly cross-shore transport mode as suggested by [17]. In the months of austral summer November 2018 to March 2019, there is a flattening or reduction in the foreshore steepness. Our data shows farther seaward shoreline locations during austral summer, which reflects the lowering of the beach slope and sediment gain. Over 25,880 m^3 of sediment is gained in the foreshore from December 2018 to March 2019 (Table 2). The main cause of

sediment gain is unclear, and the sediment transport related to beach changes may be significantly affected by the interaction between wave asymmetry and skewness [52].

For a continuous long-term study, it is recommended that a network of video camera system is used, particularly to document the predominant processes. Video cameras with high resolution will allow researchers to testify climate change and human impacts in order to improve coastal management policies and planning. However, for a single-day or short-term study, or for remote sites where it is challenging to install a camera system, a UAV system is recommended. The two systems can perform comparatively well if all the intrinsic errors are accounted for within the video camera system.

6. Conclusions

The dynamic nature of beaches requires high temporal resolution monitoring to understand the physical processes that drive change in support of coastal management. This study examined the accuracy of intertidal topographic data derived from a video camera system compared to UAV-based surveys of a reflective beach at Dzita in the Keta District. Using one year of 15-min video input and one year of monthly UAV observations, the data show good agreement ($r > 0.7$ 0) between the two systems. Intertidal profile elevations were underestimated by the video system, which was operated with a camera having a view angle. Beach slopes were found to vary between 0 and 0.7, steeper from May to July 2018 than in December 2018. Marked beach mobility occurred between August and September 2018, in response to high waves. The data suggest that long-term video measurements could enable the production of elevation data virtually as accurate as UAV products, thus rendering the video system an effective tool for coastal managers. From this research, we also conclude that UAVs are efficient for monitoring remote sites, where installing a camera system permanently, or for single-shot studies, can be challenging. It is hoped that the research work undertaken here will inform governments in building some coastal defense systems to protect beaches.

Author Contributions: For this research article the contribution of the authors is as follows: conceptualization of the paper was done by D.B.A. and P.-N.J.-Q.; methodology was developed by D.B.A. and P.-N.J.-Q.; software used were provided by D.B.A., P.-N.J.-Q. and T.C.S.; validation of results was carried by R.A. and K.A.A.; formal analysis, D.B.A., P.-N.J.-Q. and R.A.; data curation, D.B.A., P.-N.J.-Q., K.A.A. and T.C.S.; writing—original draft preparation, D.B.A.; writing—review and editing, R.A., E.J.A., and K.A.A., project administration, D.W.A. and K.A.A. All authors have read and agreed to the published version of the manuscript.

Funding: This research received funding from the National Geographic Society (grant number, CP1−07T 1−7), The World Academy of Sciences (grant Number 17429– RG/PHYS/AF/AC_IFR3240300132) and the French Embassy in Ghana. The APC was funded by The World Academy of Science (No. 17429– RG/PHYS/AF/AC_IFR3240300132) and the Institute of Research for Development (IRD) France Sud, 911 avenue Agropolis, Montpellier, France. We also want to thank the editors and the three anonymous reviewers whose comments helped to improve the manuscript.

Acknowledgments: We are grateful to the three anonymous reviewers whose comments helped to improve the manuscript. Great appreciation goes to Emmanuel Brempong and Ivy S.G. Akuoko for assisting with field work. We also thank the former assemblyman of Dzita electoral area, Sambras Dedzo and Mabel Ganah for assisting with the camera installation site and guidance of the camera. Special appreciation also goes to 'Meet Me There' Guest house management who allow us to use their premises for meetings.

Conflicts of Interest: The authors declare no conflict of interest. The funders had no role in the design of the study; in the collection, analyses, or interpretation of data; in the writing of the manuscript, or in the decision to publish the results.

References

1. Neshaei, M.A.L.; Mehrdad, M.A.; Abedimahzoon, N.; Asadollahi, N. Predicting beach profile evolution with group method data handling-type neural networks on beaches with seawalls. *Front. Struct. Civ. Eng.* **2013**, *7*, 117–126. [CrossRef]
2. Peterson, C.H.; Bishop, M.J. Assessing the Environmental Impacts of Beach Nourishment. *Bioscience* **2005**, *55*, 887–896. [CrossRef]
3. Dean, R.G.; Dalrymple, R.A. *Coastal Processes with Engineering Applications*; Cambridge University Press: Cambridge, UK, 2001.

4. Angnuureng, B.D.; Appeaning Addo, K.; Wiafe, G. Impact of sea defense structures on downdrift coasts: The case of Keta in Ghana. *Acad. J. Environ. Sci.* **2013**, *1*, 104–121. [CrossRef]
5. Jayson-Quashigah, P.N.; Appeaning Addo, K.; Kufogbe, S.K. Medium resolution satellite imagery as a tool for monitoring shoreline change. Case study of the Eastern coast of Ghana. *J. Coast. Res.* **2013**, *65*, 511–516. [CrossRef]
6. Wiafe, G.; Boateng, I.; Appeaning Addo, K.; Quashigah, P.N.; Ababio, S.D.; Laryea, S.W. *Handbook of Coastal Processes and Management in Ghana*; The Choir Press: Gloucester, UK, 2013; p. 274.
7. Holman, R.; Sallenger, A.; Lippmann, T.; Haines, J. The Application of Video Image Processing to the Study of Nearshore Processes. *Oceanography* **1993**, *6*, 78–85. [CrossRef]
8. Holland, K.; Holman, R.; Lippmann, T.; Stanley, J.; Plant, N. Practical use of video imagery in nearshore oceanographic field studies. *IEEE J. Ocean. Eng.* **1997**, *22*, 81–92. [CrossRef]
9. Anthony, E.J.; Gardel, A.; Dolique, F.; Guiral, D. Short-term changes in the plan shape of a sandy beach in response to sheltering by a nearshore mud bank, Cayenne, French Guiana. *Earth Surf. Process. Landf.* **2002**, *27*, 857–866. [CrossRef]
10. Aarninkhof, S.G.; Turner, I.L.; Dronkers, T.D.; Caljouw, M.; Nipius, L. A video-based technique for mapping intertidal beach bathymetry. *Coast. Eng.* **2003**, *49*, 275–289. [CrossRef]
11. Van Enckevort, I.; Ruessink, B. Video observations of nearshore bar behaviour. Part 1: Alongshore uniform variability. *Cont. Shelf Res.* **2003**, *23*, 501–512. [CrossRef]
12. Van Dongeren, A.; Plant, N.; Cohen, A.; Roelvink, D.; Haller, M.C.; Catalán, P.; Van Dongeren, A. Beach Wizard: Nearshore bathymetry estimation through assimilation of model computations and remote observations. *Coast. Eng.* **2008**, *55*, 1016–1027. [CrossRef]
13. Almar, R.; Ranasinghe, R.; Sénéchal, N.; Bonneton, P.; Roelvink, D.; Bryan, K.R.; Marieu, V.; Parisot, J.P. Video-Based Detection of Shorelines at Complex Meso–Macro Tidal Beaches. *J. Coast. Res.* **2012**, *28*, 1040–1048.
14. Almar, R.; Hounkonnou, N.; Anthony, E.J.; Sénéchal, N.; Mensah-Senoo, T.; Degbe, G.; Quenum, M.; Dorel, M.; Chuchla, R.; Lefebvre, J.P.; et al. The Grand Popo beach 2013 experiment, Benin, West Africa: From short timescale processes to their integrated impact over long-term coastal evolution. *J. Coast. Res.* **2014**, *70*, 651–656. [CrossRef]
15. Abessolo Ondoa, G.; Bonou, F.; Tomety, F.S.; Du Penhoat, Y.; Perret, C.; Degbe, C.G.E.; Almar, R. Beach Response to Wave Forcing from Event to Inter-Annual Time Scales at Grand Popo, Benin (Gulf of Guinea). *Water* **2017**, *9*, 447. [CrossRef]
16. Angnuureng, D.B.; Addo, K.A.; Almar, R.; Dieng, H. Influence of sea level variability on a micro-tidal beach. *Nat. Hazards* **2018**, *93*, 1611–1628. [CrossRef]
17. Angnuureng, D.B.; Jayson-Quashigah, P.N.; Addo, K.A.; Aheto, D.W.; Almar, R.; Bonou, F.; Brempong, E. Quantification of the shoreline evolution of an open beach between coastal defenses. In Proceedings of the 9th International Conference in Coastal Sediments, Petersburg, FL, USA, 27–31 May 2019; pp. 1562–1576.
18. Bonou, F.; Angnuureng, D.B.; Sohou, Z.; Almar, R.; Alory, G.; Du Penhoat, Y. Shoreline and Beach Cusps Dynamics at the Low Tide Terraced Grand Popo Beach, Bénin (West Africa): A Statistical Approach. *J. Coast. Res.* **2018**, *81*, 138–144.
19. Colomina, I.; Molina, P. Unmanned aerial systems for photogrammetry and remote sensing: A review. *ISPRS J. Photogramm. Remote Sens.* **2014**, *92*, 79–97. [CrossRef]
20. Anderson, K.; Westoby, M.J.; James, M.R. Low-budget topographic surveying comes of age: Structure from motion photogrammetry in geography and the geosciences. *Prog. Phys. Geogr. Earth Environ.* **2019**, *43*, 163–173. [CrossRef]
21. Klemas, V.V. Coastal and Environmental Remote Sensing from Unmanned Aerial Vehicles: An Overview. *J. Coast. Res.* **2015**, *315*, 1260–1267. [CrossRef]
22. Bergsma, E.W.; Almar, R.; De Almeida, L.P.M.; Sall, M. On the operational use of UAVs for video-derived bathymetry. *Coast. Eng.* **2019**, *152*, 103527. [CrossRef]
23. Brunier, G.; Fleury, J.; Anthony, E.J.; Gardel, A.; Dussouillez, P. Close-range airborne Structure-from-Motion Photogrammetry for high-resolution beach morphometric surveys: Examples from an embayed rotating beach. *Geomorphology* **2016**, *261*, 76–88. [CrossRef]

24. Pitman, S.J.; Hart, D.E.; Katurji, M.H. Beach Cusp Morphodynamics on a Composite Beach Observed Using UAV Structure from Motion. In Proceedings of the Australian Coasts and Ports Conference, Hobart, Autralia, 10–13 September 2019.
25. Laporte-Fauret, Q.; Marieu, V.; Castelle, B.; Michalet, R.; Bujan, S.; Rosebery, D. Low-Cost UAV for High-Resolution and Large-Scale Coastal Dune Change Monitoring Using Photogrammetry. *J. Mar. Sci. Eng.* **2019**, *7*, 63. [CrossRef]
26. Agüera-Vega, F.; Carvajal-Ramírez, F.; Martínez-Carricondo, P. Assessment of photogrammetric mapping accuracy based on variation ground control points number using unmanned aerial vehicle. *Measurement* **2017**, *98*, 221–227. [CrossRef]
27. Anthony, E.; Almar, R.; Aagaard, T. Recent shoreline changes in the Volta River delta, West Africa: The roles of natural processes and human impacts. *Afr. J. Aquat. Sci.* **2016**, *41*, 81–87. [CrossRef]
28. Kutu, J.M. Seismic and Tectonic Correspondence of Major Earthquake Regions in Southern Ghana with Mid-Atlantic Transform-Fracture Zones. *Int. J. Geosci.* **2013**, *4*, 1326–1332. [CrossRef]
29. Davies, J.L. *Geographical Variation in Coastal Development*, 2nd ed.; Longman: London, UK, 1980; p. 212.
30. Almar, R.; Kestenare, E.; Reyns, J.; Jouanno, J.; Anthony, E.J.; Laibi, R.; Hemer, M.; Du Penhoat, Y.; Ranasinghe, R. Response of the Bight of Benin (Gulf of Guinea, West Africa) coastline to anthropogenic and natural forcing, Part 1: Wave climate variability and impacts on the longshore sediment transport. *Cont. Shelf Res.* **2015**, *41*, 81–87. [CrossRef]
31. Boateng, I. Development of Integrated Shoreline Management Planning: A Case Study of Keta, Ghana Development of Integrated Shoreline Management Planning: A Case Study of Keta, Ghana. In *Federation of International Surveyors Working Week 2009, Surveyors Key Role in Accelerated Development*; International Federation of Surveyors: Eilat, Israel, 2019; pp. 1–19.
32. Ly, C.K. The role of the Akosombo Dam on the Volta river in causing coastal erosion in central and eastern Ghana (West Africa). *Mar. Geol.* **1980**, *37*, 323–332. [CrossRef]
33. Anthony, E.; Blivi, A. Morphosedimentary evolution of a delta-sourced, drift-aligned sand barrier–lagoon complex, western Bight of Benin. *Mar. Geol.* **1999**, *158*, 161–176. [CrossRef]
34. Anthony, E.J.; Almar, R.; Besset, M.; Reyns, J.; Laibi, R.; Ranasinghe, R.; Abessolo Ondoa, G.; Vacchi, M. Response of the Bight of Benin (Gulf of Guinea, West Africa) coastline to anthropogenic and natural forcing, Part 2: Sources and patterns of sediment supply, sediment cells, and recent shoreline change. *Cont. Shelf Res.* **2019**, *173*, 93–103. [CrossRef]
35. Westoby, M.; Brasington, J.; Glasser, N.; Hambrey, M.; Reynolds, J. 'Structure-from-Motion' photogrammetry: A low-cost, effective tool for geoscience applications. *Geomorphology* **2012**, *179*, 300–314. [CrossRef]
36. Snavely, N. Scene Reconstruction and Visualization from Internet Photo Collections: A Survey. *IPSJ Trans. Comput. Vis. Appl.* **2011**, *3*, 44–66. [CrossRef]
37. Agisoft. Agisoft PhotoScan. Available online: http://www.agisoft.com/ (accessed on 15 April 2018).
38. Mancini, F.; Dubbini, M.; Gattelli, M.; Stecchi, F.; Fabbri, S.; Gabbianelli, G. Using Unmanned Aerial Vehicles (UAV) for High-Resolution Reconstruction of Topography: The Structure from Motion Approach on Coastal Environments. *Remote Sens.* **2013**, *5*, 6880–6898. [CrossRef]
39. Furukawa, Y.; Ponce, J. Accurate, dense, and robust multi-view stereopsis. *IEEE Trans. Pattern Anal. Mach. Intell.* **2010**, *32*, 1362–1376. [CrossRef] [PubMed]
40. Wheaton, J.M.; Brasington, J.; Darby, S.E.; Sear, D.A. Accounting for uncertainty in DEMs from repeat topographic surveys: Improved sediment budgets. *Earth Surf. Process. Landf.* **2010**, *35*, 136–156. [CrossRef]
41. Boak, E.H.; Turner, I.L. Shoreline Definition and Detection: A Review. *J. Coast. Res.* **2005**, *214*, 688–703. [CrossRef]
42. Copernicus Climate Change Service, C3S. ERA5: Fifth Generation of ECMWF Atmospheric Reanalyses of the Global Climate; Copernicus Climate Change Service Climate Data Store (CDS). Available online: https://cds.climate.copernicus.eu/cdsapp#!/home (accessed on 12 August 2019).
43. The Wamdi Group. The WAM Model—A Third Generation Ocean Wave Prediction Model. *J. Phys. Oceanogr.* **1988**, *18*, 1775–1810. [CrossRef]
44. Flater, D. WXTide32—A Free Windows Tide and Current Prediction Program. Available online: www.wxtide32.com (accessed on 25 September 2018).
45. Thieler, R.E.; Himmelstoss, E.A.; Zichichi, J.L.; Ergul, A. The Digital Shoreline Analysis System (DSAS) Version 4.0, An ArcGIS Extension for Calculating Shoreline Change (ver. 4.4, July 2017). 2017, U.S. Geological

Survey Open-File Report. 2008-1278. Available online: https://searchworks.stanford.edu/view/8366174 (accessed on 12 August 2019).
46. Klein, A.H.F.; Menezes, J.T. Beach morphodynamics and profile sequence for a headland. *J. Coast. Res.* **2001**, *17*, 812–835.
47. Almar, R.; Almeida, P.; Blenkinsopp, C.; Catalan, P. Surf-swash interactions on a low-tide terraced beach. *J. Coast. Res.* **2016**, *75*, 348–352. [CrossRef]
48. Athanasiou, P.; van Dongeren, A.; Giardino, A.; Vousdoukas, M.; Gaytan-Aguilar, S.; Ranasinghe, R. Global distribution of nearshore slopes with implications for coastal retreat. *Earth Syst. Sci. Data* **2019**, *11*, 1515–1529. [CrossRef]
49. Bergsma, E.W.J.; Conley, D.C.; Davidson, M.A.; O'Hare, T.J.; Almar, R. Storm Event to Seasonal Evolution of Nearshore Bathymetry Derived from Shore-Based Video Imagery. *Remote Sens.* **2019**, *11*, 519. [CrossRef]
50. Young, I. Seasonal variability of the global ocean wind and wave climate. *Int. J. Clim.* **1999**, *19*, 931–950. [CrossRef]
51. Stive, M.J.; Aarninkhof, S.G.; Hamm, L.; Hanson, H.; Larson, M.; Wijnberg, K.M.; Nicholls, R.J.; Capobianco, M. Variability of shore and shoreline evolution. *Coast. Eng.* **2002**, *47*, 211–235. [CrossRef]
52. Plant, N.G.; Holman, R.A. Intertidal beach profile estimation using video images. *Mar. Geol.* **1997**, *140*, 1–24. [CrossRef]